Title

Influence of Standard Image Processing of 3D X-ray Microscopy on Morphology, Topology and Effective Properties

Journal

Energies, 15(20)

ISSN

1996-1073

Authors

Guibert, Romain

Nazarova, Marfa

Voltolini, Marco

et al.

Publication Date

2023-12-14

DOI

10.3390/en15207796

energies

MDPI

Article

Influence of Standard Image Processing of 3D X-ray Microscopy on Morphology, Topology and Effective Properties

Romain Guibert [1], Marfa Nazarova [2], Marco Voltolini [3,4], Thibaud Beretta [2], Gerald Debenest [1] and Patrice Creux [2,*]

[1] Institut de Mécanique des Fluides de Toulouse (IMFT), Université de Toulouse, CNRS-INPT-UPS, 31400 Toulouse, France
[2] Université de Pau et des Pays de l'Adour, E2S UPPA, CNRS, TotalEnergies, LFCR, 64000 Pau, France
[3] Earth and Environmental Sciences Area, Energy Geoscience Division, Lawrence Berkeley National Laboratory, 1 Cyclotron Road, Berkeley, CA 94720, USA
[4] Sezione di Mineralogia, Dipartimento di Scienze della Terra "Ardito Desio", Università degli Studi di Milano Statale, Via Botticelli 23, 20133 Milano, Italy
* Correspondence: patrice.creux@univ-pau.fr; Tel.: +33-559-407-681

Abstract: Estimating porous media properties is a vital component of geosciences and the physics of porous media. Until now, imaging techniques have focused on methodologies to match image-derived flows or geomechanical parameters with experimentally identified values. Less emphasis has been placed on the compromise between image processing techniques and the consequences on topological and morphological characteristics and on computed properties such as permeability. The effects of some of the most popular image processing techniques (filtering and segmentation) available in open source on 3D X-ray Microscopy (micro-XRM) images are qualitatively and quantitatively discussed. We observe the impacts of various filters such as erosion-dilation and compare the efficiency of Otsu's method of thresholding and the machine-learning-based software Ilastik for segmentation.

Keywords: porous media; pore scale; image processing; segmentation; computed micro-X-ray microscopy; effective properties; digital rock physics

Citation: Guibert, R.; Nazarova, M.; Voltolini, M.; Beretta, T.; Debenest, G.; Creux, P. Influence of Standard Image Processing of 3D X-ray Microscopy on Morphology, Topology and Effective Properties. *Energies* **2022**, *15*, 7796. https://doi.org/10.3390/en15207796

Academic Editor: Mofazzal Hossain

Received: 5 August 2022
Accepted: 17 October 2022
Published: 21 October 2022

1. Introduction

The purpose of Digital Rock Physics (DRP) is to predict the effective properties of rock by imaging a medium and running calculations to estimate those properties at the pore scale. Moreover, to analyze in situ mechanisms at the pore scale (wettability, snap-off, etc.), imaging techniques are used to reveal fluid distribution, the shapes of the interfaces between fluids, and the gradients relative to sub-voxel size. Image processing is a decisive step in resolving pore space in order to build accurate models and enhance our knowledge of mechanisms [1–5]. In previous works, we revealed the limitations, or at least the precautions required, in terms of mesh size [6] and spatial resolution [7] when performing single-phase flow simulations. High-resolution images provide detailed information on rock microstructures and fluid distribution. The researcher produces images at a selected voxel size that is considered to be the best compromise between spatial resolution and the Representative Elementary Volume for averaging all of the local heterogeneities, and generates a sample volume that is representative of homogenous properties [8].

Multiphase flow characteristics are strongly dependent on image resolution and gridding, which is why the upscaling process based on pore-scale simulations is crucial for predicting low-resolution model properties regarding the aforementioned compromise. Certain specific algorithms claim to represent flow at several resolutions, but are not scalable in image-based contexts, which limits their use to multi-resolution simulations.

Please note that there is no evidence that the multi-scale approach is valid at the pore scale, because a larger field of view is required to average the properties due to the presence

of heterogeneities. As a consequence, the larger field of view drastically impacts image processing and simulations owing to the huge demand of cubic law on computing power.

Kaestner et al. [9] described the effects of different image processing filters on images obtained using synchrotron 3D X-ray microscopy. The main image-processing approaches (image filtering and segmentation) were described by Schlüter et al. [10]. Iassonov [11] proposed a complete review of several new and accurate segmentation algorithms for X-ray images. Sheppard et al. [12] described the qualitative effects of filtering and segmentation. Many innovative image enhancing methods deserve to be tested [13,14] along with more advanced A.I. algorithms for super resolution or segmentation via semantic algorithms [15], but the main objective here was to assess what currently exists and to qualitatively and quantitatively estimate the impact of image processing in order to propose a complete methodology linked to the uncertainty calculations in Digital Rock Physics.

Concerning the impacts of these methods, Andrä et al. [16,17] first proposed numerically measuring the effective properties based on several complete workflows presenting relatively small differences in porosity (2.5%) and converging the results on other properties, irrespective of the technique used in the tests performed by any one of the three teams. We compared the direct impacts of image processing and segmentation on the porosity value of the sample.

This is a very limited bibliography concerning the study of the effects of image processing from the micro to the macro scale. Saxena et al. [18] did the same for several (Otsu vs. fuzzy c-means (FCM) algorithms) segmentation methods.

Here, we will estimate the direct impact of image processing on the morphology, topology and effective properties of the porous media while respecting the reliability conditions demonstrated previously [6,7], and we will attempt to corroborate local images with these macro-computed properties in order to determine the impact of each filter and segmentation algorithm on the porous media structures and fluid distributions, and consequently on the degradation of image quality with a reduction in contrast.

2. Materials and Methods

2.1. Image Acquisitions

The sandstone core used in this study was collected in the Domengine formation, and more specifically from a gallery in the Hazel-Atlas Mine at Black Diamond Mine Regional Park (Antioch, CA, USA). For the X-ray μCT imaging, a cylindrical core plug, 9 mm in diameter and 20 mm long, was drilled.

For the two-phase flow experiments, we used 0.1 M of potassium iodide (KI) in water as a contrast agent. The concentration of 0.1 M KI in the water forms a brine with intermediate XR attenuation values between the $scCO_2$ and the quartz and therefore provides the ideal gray-level contrast required to separate the different phases. The single-phase and two-phase flow experiments were performed on Beamline 8.3.2 at the Advanced Light Source (ALS) at the Lawrence Berkeley National Laboratory. The entire set-up and methodology were previously described by Voltolini et al. [19]. For the two-phase flow of $scCO_2$, the images were collected on the core plug, and experiments were successively performed on the same sample in the same position. The complete dataset is a stack of 853 slices of 2650 × 2414 with a voxel size of 4.4 μm. Images were cropped to 800 × 800 × 800 voxels and were processed using a fully assembled computer with a 12-core Intel® Core™ i7-5820K CPU @ 3.30 GHz, with 32 Gigabytes of RAM and an NVIDIA GM204 GPU under Ubuntu 18.04.6.

2.2. Image Processing

A numerical filter inserted into the feedback path of a control loop can reduce the noise that often corrupts the process of gray-level recognition (identification of minerals and morphology/topology).

Image filtering is a standard step that is mentioned in most articles on pore-scale imaging in the geoscience field. To avoid redundancy, we considered two groups of common filters.

The first group associates the median filter and the mean filter. The median filter smooths images by replacing each voxel with the median value of its neighbors, and the mean filter replaces each voxel with the mean value of its neighbors; the central gray level is then compared with the surrounding voxels to estimate the matching. These filters are very efficient on salt-and-pepper noise, random noise, and Gaussian noise, without the smoothing effects that can occur with other types of smoothing filters. By definition, these filters are very local, because the correction is performed only from direct neighbors. In the second group, however, filtering was performed on part of the slice.

The Anisotropic Diffusion, Bilateral and Non-Local Means filters are global filters that analyze a large number of voxels to constrain image filtering by means of equations or probabilities as it strongly affects histograms at phase scale.

In anisotropic diffusion, the gray level and the interfacial gradient between two phases are constrained by the diffusion equation. The intensity of each pixel is replaced by a weighted average of nearby pixel intensity values and the non-local means smooth images by taking a mean of all pixels, weighted by how similar the pixels are to the target pixel.

The second group of filters has a strong impact, affecting the gray-level distribution and the contrasts between materials. We therefore did not want to use them in combination with Ilastik due to the severe corrections to the histograms, which modify much more than random white noise.

The association of this second group of filters with Otsu's method for thresholding features in most of the published articles on image processing applied to 3D X-ray imaging in the field of the physics of porous media.

When using these traditional image processing workflows in complex environments, the operator is faced with compromises and, therefore, choices. The human eye combined with analyses clearly achieve better identification than standard segmentation methods based on histogram thresholding of gray-level images. X-ray detectors ideally (without any artefacts) fit a Gaussian curve to the histogram centered on the attenuation value of the material. The presence of multiple materials, as are usually found in geosciences, causes an overlap between the characteristic peaks, with the consequence being that materials are eroded or dilated when segmentation is performed using only a thresholding method.

In addition to the microtomographic artefacts causing refractions, beam hardening, low contrast between two materials—when the detail observed is of the same order of magnitude or smaller than the voxel size—or even uncertainties related to the non-uniqueness of the tomographic reconstruction for a finite number of X-rays can also cause artefacts originating in the overlap of the Gaussian peaks of different materials. The Australian National University (ANU) proposed several histogram decomposition algorithms based on this physical concept. The present study was based on the observation that the human eye and brain are able to gauge an error by comparing the raw and filtered images and segmenting them using the same process. A trained eye, however, can only employ a qualitative approach. The method proposed here consists of identifying the workflow that will achieve the best conformity between the raw image and the segmented image at the pore space level using this traditional qualitative approach.

Preliminary work plainly showed a significant difference between Ilastik and the other workflows, with a clear advantage for Ilastik in both pore space recognition and multi-material recognition. We therefore selected Ilastik as a reference in this work and qualitatively and quantitatively measured the differences between processing and the impact on the properties of the porous media.

Machine learning software [20] is used to extend the number of identification criteria in the same way as the human brain. For anyone who has processed images obtained by 3D X-ray tomography, finding the best filter during the processing phases by playing with the associated tuning parameters and reiterating the approach for thresholding is subjective,

leading to human inferences in the choice of the best compromise. The possibility of obtaining a correct segmentation of standard processing is therefore limited to some very distinct gray levels between phases. In the sample chosen, for example, fluids are associated with very smooth shapes and macroscopic curvatures, representing criteria additional to contrast and gray levels during the pixel classification phase. For example, the gray levels of doped water and smectites are almost identical, and only Ilastik or equivalent tools are able to separate objects with peak overlapping. Automation of the entire image processing workflow in a deep learning process is therefore not yet mature but it could be quite interesting for reducing image processing time and controlling errors in images. Ilastik was selected for its efficiency compared to that of the software generally used in this field. Ilastik is open-source software, which in a preliminary phase demonstrated highly effective image labeling without ever producing confusing results, whatever the gray levels.

Of course, there are many more advanced filtering and segmentation algorithms, and it is impossible to list them all. There are some very promising image-quality enhancers, filters, and segmentation algorithms, but they remain a niche technique in a field of application that generally uses basic methods. Among them, we could mention the Hybrid no-reference quality metric for singly and multiply distorted images, A fast reliable image quality predictor by fusing 2 micro- and macro-structures, filtering structured artefacts using suitable algorithms and segmentation generated using certain semantic segmentation methods, Image Segmentation by Data-Driven Markov Chain Monte Carlo, and many others. The methodology proposed here, however, is a selective method able to estimate the efficiency of the entire image processing workflow. The four different filters are among those most commonly used by scientists working on the physics of porous media and are usually freely available using the open-source codes in the image processing program ImageJ.

2.2.1. Filtering

Mean filtering entails replacing the value of each pixel in an image with the mean gray values of its neighbors and itself. It has the effect of eliminating pixel values that are unrepresentative of their surroundings. Mean filtering is a convolution filter based on a simple sliding-window spatial filter (n by n window matrix with n being an odd number).

The median filter is a sliding-window spatial filter, which replaces the value of each pixel in the image with the median of the neighboring pixel values. The median is calculated first by sorting all the pixel values from the surrounding neighborhood into numerical order then replacing the given pixel with the averaged pixel value.

The bilateral filter is a weighted average filter. It weighs the central pixel and is calculated from two contributions: spatial and range weights. Its efficiency is therefore enhanced, because both the spatial distance between the pixels examined and their intensity similarity are considered [21].

The non-local means filter [2] is an algorithm that takes the mean value of a group of pixels surrounding a target pixel to smooth the image; the value is weighted by how similar those pixels are to the target pixel. This filter appears quite interesting when the operator exploits the image using sufficient contrast in the imaged composite rock. The result is usually improved image clarity and a minor loss of detail compared with the traditional local mean filter.

The anisotropic diffusion process here is based on the use of a nonlinear filter. Perona and Malik [22] proposed a nonlinear diffusion method to avoid the blurring and localization problems posed by linear diffusion filtering. The anisotropic diffusion filter is one of the most commonly used denoising filters for dry rock images [12] obtained by X-ray tomography, and there are consequently some strong gray-level gradients between the pore space and minerals.

Several denoising filters can be applied to computed tomography images, but in this case, we consider only those most often mentioned in the literature. The filters of group 2 act at the phase scale, and can therefore correct the gray levels and contrasts between materials.

For this reason, we did not want to use them in combination with Ilastik due to the severe corrections to the histograms, which modify much more than random white noise.

2.2.2. Segmentation

In our context of Digital Rock Physics, however, our aim is not only to perform phase identification, but also to accurately preserve the morphologies of the objects in the different classes, including the boundaries between the pore space/fluids and the minerals or between the grains themselves, in order to obtain the most mimetic representation of the rock sample, saturated or not.

In an image processing workflow, the process that follows denoising is segmentation, i.e., phase/mineral separation performed by thresholding in manual (global thresholding) or semi-automatic mode (Otsu thresholding). Global thresholding is the simplest segmentation method: the voxels with values above a certain threshold are assigned the properties of a dense mineral, and those with values below a fixed threshold are assigned the properties of other materials, such as those of a different mineral, or pore phases, or air or water [23]. On the other hand, automatic thresholding involves automatically selecting one or more optimal gray-level threshold values for separating objects, which is the premise of Otsu's method.

The algorithm performs thresholding slice by slice, with the main advantage being that it considers the source drift, and the spectral and spatial characteristics of off-focal radiation.

With the large number of free libraries available, and the increase in computing capacities, Artificial Intelligence has given rise a new generation of image processing tools such as Weka [24] and Ilastik [25,26].

We investigated these free, open-source software programs and compared them to the more conventional workflows involving pre-filtering and segmentation.

The Weka (Waikato Environment for Knowledge Analysis [24]) classifier for 2D and 3D images, which combines a series of machine learning algorithms with a set of selected image features, proved quite efficient [27]. There are many common options for classifiers, most of which are related to evaluation. The following features are available in Trainable Weka Segmentation: edge detectors, the aim of which is to indicate the object boundaries in an image (e.g., Laplacian and Sobel filters, difference of Gaussians, Hessian matrix eigenvalues and Gabor filters); texture filters, to extract texture information (including filters such as minimum, maximum, median, variance, entropy, structure tensor, etc.); and noise reduction filters, such as Gaussian blur, bilateral, Anisotropic diffusion, Kuwahara and Lipschitz.

Ilastik [25] includes certain improvements, and pixel classification may be reinforced by object classification. Pixel classification features may include pixel/color intensity, if color or brightness can be used to discern objects, or edge detectors for brightness or color gradients, serving to discern objects and textures if the image has a special textural appearance. In addition to pixel classification, object classification features are subdivided into three groups: "Location", "Shape", and "Intensity Distribution". Location-based features consider the absolute coordinate positions in the image. These are useful only in specific cases when the position of the object in the image can be used to infer the object type. Shape-based features extract shape descriptors from the object masks. Lastly, "Intensity Distribution" features operate on image value statistics. One can also observe features, which can be computed in the vicinity of the object, found by distance transform, and the features are computed for the object itself and for the surrounding area including and excluding the object. In this work, Ilastik was selected as the reference for segmentation, in standalone mode without any filtering.

2.2.3. Methodology

The effects of the previously described filters were compared by applying overlapping masks on the raw image to locally identify tendencies in a specific part of the 3D dataset, and by performing segmentation using Otsu's method to extract the pore space. Binarization

was necessary to numerically determine the morphological and topological properties strongly impacting flow in porous media.

We decided to perform segmentation using multi-Otsu thresholding, which is based on intensity histograms, and pixel intensity classification is the basic characteristic used in image filtering.

Our goal during observation was therefore to determine whether or not certain additional elements would significantly increase image quality. Please note that Artificial Intelligence methods can be used on raw images, meaning that they can be used to correct noise reduction and certain types of artifacts due to the large number of classifiers.

The ability to preserve the pore-space characteristics (morphology and topology) affects the characteristic terms and transport properties. Several calculated topological, morphological and transport properties were selected to be extrapolated to the entire core plug.

We chose to label smectites as non-contributing to flow, based on the assumption that water remains bound to this type of mineral and therefore contributes little or nothing to the flow. Because of the very good match between the segmentations performed on dry rock images in two-phase conditions, we will be comparing, in the next part, the impacts of all of the filters on the Domengine sample in two-phase conditions to take advantage of the additional attenuations and interfaces in the porous medium.

Filtering was performed by exaggerating the filter line somewhat and then softening its effect until an image was obtained in which segmentation can play its role. Filtering is, therefore, light. After the images had been filtered and segmented, the results were compared, showing that the measured porosities were very close—an average value of 18.61% and a maximum difference of 0.33%. The objective here was to filter the images without impacting the edges (the gray-level gradients) and thereby maintain the boundaries (by finding the best compromise among the filter parameters).

The consequence of filtering is a systematic erosion/dilation and the loss of the tightest pores).

To represent the impact of image processing and segmentation, we created a graphical representation considering a reference image 1: R_1 (for example, mean filtering and Otsu's method); and a reference image 2: R_2 (raw image segmented using Ilastik).

The images presented were generated using the following successive logic functions:

The yellow mask was given by $R_1 \cap (R_1 \oplus R_2) = Y$ and the blue mask by $R_2 \cap (R_1 \oplus R_2) = B$.

The graphs shown here were obtained by superimposing the two masks over the raw image to observe tendencies.

2.2.4. Numerical Evaluations

To assess the different image processing techniques selected, we compared both intrinsic values (porosity and specific surface area) and numerical evaluations using specific methods (coordination number and permeability).

The cubic computational volume considered for these post-processing measurements consisted of $852 \times 852 \times 852$ voxels.

To evaluate the coordination number, i.e., the number of incident paths to a pore, we had to construct a skeleton of the binarized image. The value evaluated could depend on the algorithm used; here, we used the CImg library [28,29].

To evaluate permeability, we used the standard finite-volume library OpenFOAM and reproduced a permeameter configuration for each direction. We used a SIMPLE algorithm to solve the steady-state Navier–Stokes equations with second-order discretization schemes in space.

3. Results

3.1. Numerical Results

In this first part of the results, we quantitatively compare the results without filtering and segmenting them with Ilastik. In this section, we show the effect of the filters with some images and macroscopic indicators. The complete results are presented in Table 1 and in Figure 1.

Table 1. Porosity and normalized porosity, specific surface area, coordinance and permeability for the different filter/segmentation-tested couples with the reference, considered as Otsu thresholding of the raw image expressed in voxels and %.

Nature of the Filter	Segmentation	Porosity %	Specific Surface Area (1/m)	Coordinance	K_{xx} ($\times 10^{12}$ m^2)	K_{yy} ($\times 10^{12}$ m^2)	K_{zz} ($\times 10^{12}$ m^2)
Raw image	Otsu	22.08	19,615	5.60	4.86	5.18	4.21
Median	Otsu	21.88 (0.87%)	16,971 (−13.48%)	4.85 (−13.33%)	5.57 (+14.60%)	5.95 (+14.85)	4.60 (+9.21%)
Mean	Otsu	2 (−0.36%)	17,183 (−12.40%)	5.08 (−9.17%)	5.50 (+13.15%)	5.89 (+13.66%)	4.63 (+10.07%)
Bilateral	Otsu	22.7 (+0.89%)	18,516 (−5.60%)	5.10 (−8.96%)	5.33 (+9.74%)	5.69 (+9.86%)	4.58 (+8.73%)
Non-local means	Otsu	22.54 (+2.09%)	19,317 (−1.52%)	5.38 (−3.95%)	5.35 (+10.03%)	5.72 (+10.40%)	4.64 (+10.23%)
Anisotropic Diffusion	Otsu	22.19 (+ 0.53%)	18,936 (−3.46%)	5.26 (−6.07%)	5.12 (+5.35%)	5.47 (+5.52%)	4.42 (+5.12%)
Raw image	Ilastik	24.57 (+11.30%)	25,312 (29.05%)	6.57 (+17.34%)	6.04 (+24.26%)	6.27 (+21.12%)	5.50 (+30.59%)
Anisotropic Diffusion	Ilastik	24.55 (+11.18%)	25,940 (+32.25%)	6.61 (+18.14%)	6.21 (+27.66%)	6.44 (+24.36%)	5.60 (+33.34%)

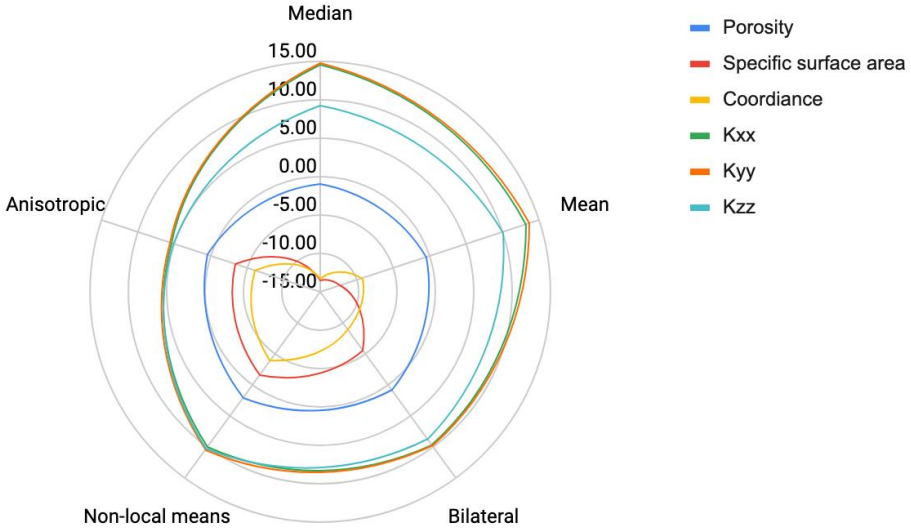

Figure 1. Impact of filtering and segmentation on effective properties. The different filtered 3D images segmented using Otsu are normalized with the Ilastik segmentation.

3.2. Raw Otsu vs. Ilastik

Comparison of the various segmentations performed directly on the raw data using either Otsu's method or Ilastik revealed the first interesting differences. Indeed, Otsu's method allows adjustments, and therefore attains the best compromise in terms of segmentation according to the rendering. Porosities differ by more than 10%. Among the different voxels, Otsu favors erosion, mainly around wedges and edges (Figure 2), but Ilastik is

much more efficient for identifying the different phases, and the gray-level gradient is not the only impacting parameter. Ilastik is much more efficient for detecting the details of small pores.

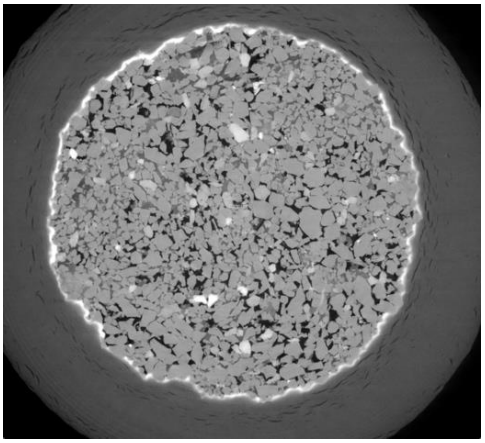

(**a**)

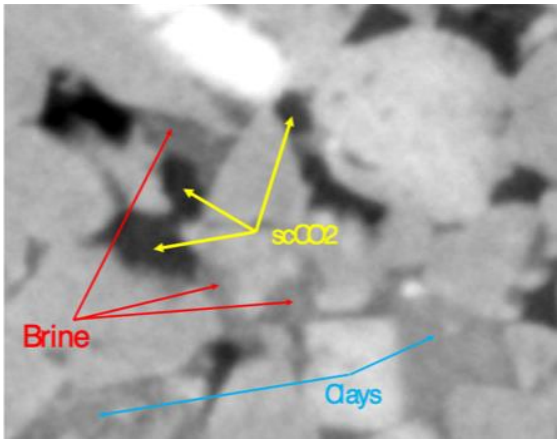

(**b**)

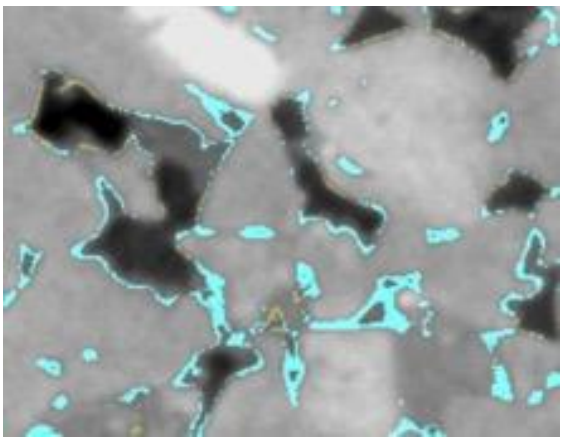

(**c**)

Figure 2. Influence of the segmentation performed with Ilastik vs. Otsu's method: (**a**) raw reconstructed image, (**b**) description of a local zoom with an identification of phases, (**c**) local zoom with cyan voxels corresponding to voxels considered to represent porosity only using Ilastik (relative to Otsu's thresholding), and yellow voxels corresponding to voxels considered to represent porosity only using Otsu's thresholding (relative to Ilastik).

Segmentation performed using Otsu's thresholding produces a porosity 11% lower, a coordinance number 18% lower, a surface specific area of 32% lower and a permeability up to 30% lower in the vertical range, producing a higher error compared to Ilastik, which in our view provides the best segmentation. On the other hand, the macroscopic indicators of specific surfaces and connections are better preserved, but locally there are some significant mismatches in morphology and topology. Structured defects generate non-existing pores and small pores associated with low gray gradients in the image, which are not considered to have a significant impact on segmentation. There are substantial differences between the direct segmentations performed using the Otsu's method and Ilastik algorithms, especially in some areas where the difference in gray levels does not distinctly highlight the contrast between phases. Here, we illustrate the main issue of the standard segmentation method, where gray continuity in the histogram requires the user to perform a subjective cut-off of the various phases considering a spectral continuum. The question here is whether the use of a filter can improve Otsu segmentation to make it more efficient or even comparable to the results provided by Ilastik.

3.3. Pre-Filtering Ilastik vs. Ilastik

A pre-filtering step performed before the segmentation with Ilastik had a slight impact on the different indicators—0.1% on porosity, 2.6% on the specific surface area, 7% on the coordination number, and a maximum of 2.6% on permeability. Filtering smoothed some independent pixels, but the impact was virtually non-existent, meaning that a filtering step when using Ilastik is pointless, as shown on a cropped numerical sample (Figure 3).

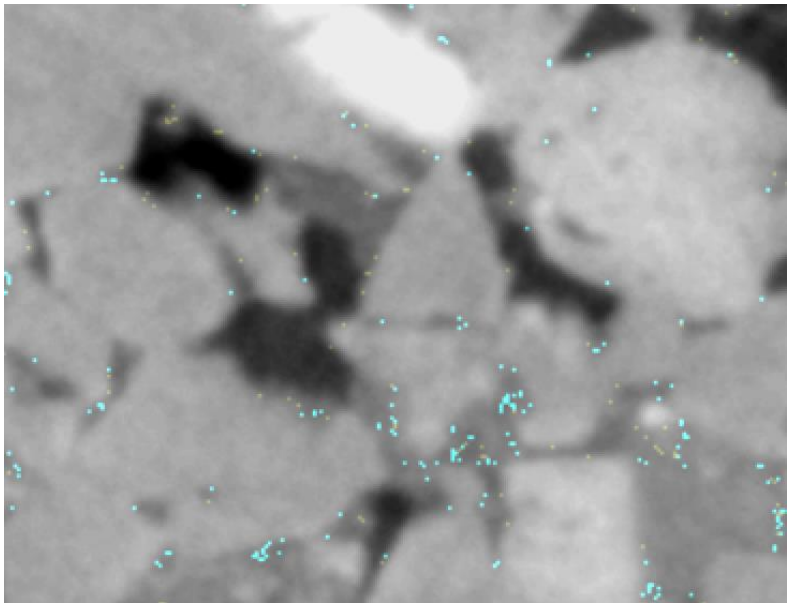

Figure 3. Raw image with a superposed representation of "additional" pore space voxels in cyan of a raw image and "missing" pore space with an Ilastik segmentation compared to when prefiltered with Anisotropic Diffusion and Ilastik segmentation.

3.4. Mean and Median Filtering vs. Ilastik

The mean and median filters associated with Otsu's method displayed an error range of about 10% for porosity. However, the surface area, as well as the x-, y- and z-permeability properties ranged from 19,615 m^{-1} to 25,312 m^{-1} (a difference of about 20%) and from 4.86×10^{-12} m^2 to 6.04×10^{-12} m^2; 5.18×10^{-12} m^2 to 6.27×10^{-12} m^2 and 4.21 to 5.50×10^{-12} m^2 (with a maximum difference of around 31%) compared to segmentation using Ilastik (Table 1). A cropped sample shows the differences (Figure 4) between the two. Despite some very similar macroscopic values, there are some substantial local differences in the case of edges and wedges.

The median and mean filters exhibited limitations in terms of preserving edges and corners and generated step marching. They presented the greatest differences with Ilastik in terms of the specific surface area and permeability.

The mismatches observed when using the filters were mainly due to Otsu's method's inability to accurately distinguish between two materials with similar gray levels. Since the passage of X-rays through a homogeneous material causes a Gaussian peak for each material on the generated image, ANU suggested using this property to deconvolute the individual material peaks from the complete histogram. In our case, the overlap between neighboring peaks is not managed using the erosion–dilation system. It is difficult to distinguish clays from brine using only an Otsu algorithm. There is no intrinsic watershed, meaning that the contrast is obtained from gradients originating from low-contrast phases.

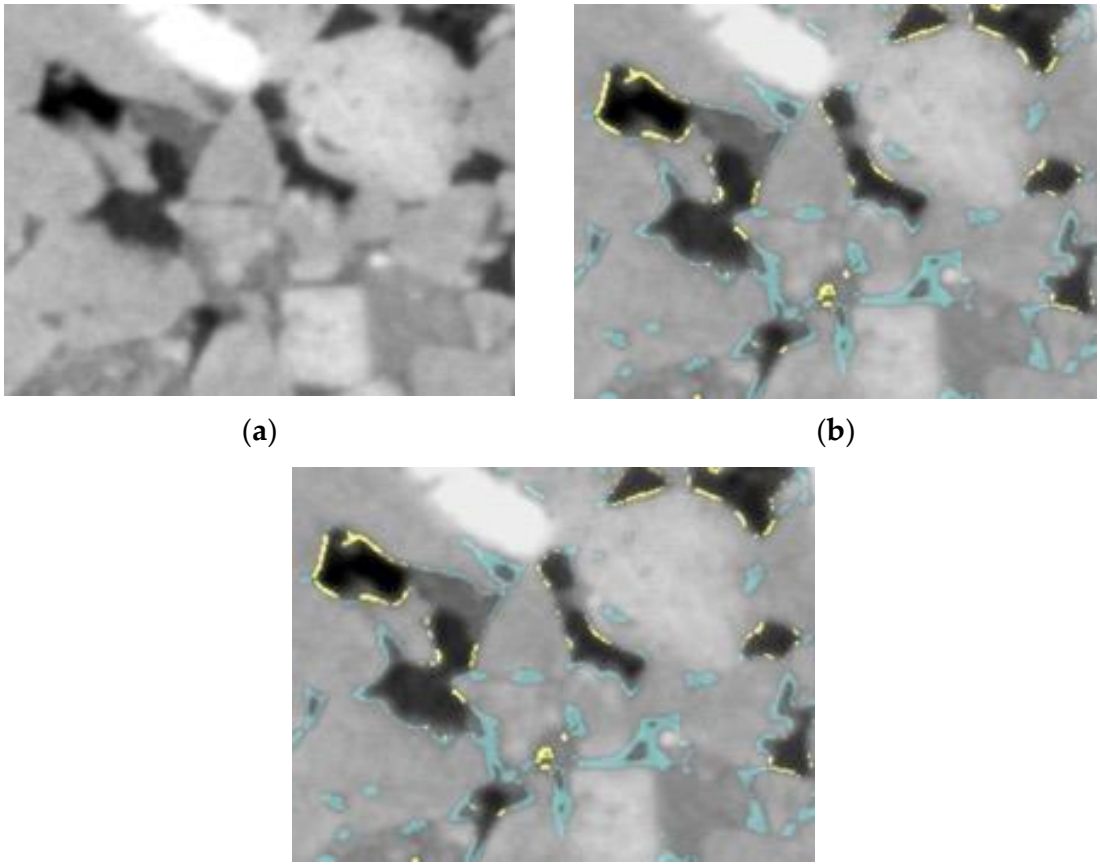

Figure 4. Impact and comparison at the local scale of the mean and median filtering with Otsu's thresholding compared to Ilastik: (**a**) the raw reconstructed image with the impact of (**b**) mean filtering and (**c**) median filtering (right). Local zooms with the voxels corresponding to voxels considered to represent porosity with Ilastik only (relative to the cited filter + Otsu's thresholding) in cyan; and with voxels corresponding to voxels considered to represent porosity with the cited filter associated with Otsu's thresholding only (relative to Ilastik) in yellow.

3.5. Bilateral, Anisotropic Diffusion and Non-Local Means vs. Ilastik

The main difference observed with these filters was an enhanced description of specific surface area, 9% higher than with median and mean filters. However, edge and wedge mismatches had a negative impact on the results. Some tight pores and pore-throat conformance are poorly represented. Some of the permeability calculations on the simulation differ by 3 to 4% compared to the mean and median filters, despite a coordination number 5% higher. Locally, Figure 5 shows the effects of these filters on a cropped 3D image.

This study sought to quantify the impact of image processing on effective properties using a standard filtering and segmentation process versus the use of A.I. software, making it possible to perform multi-label segmentation and not just gray-level segmentation. The results show that, thanks to its multi-label algorithm, Ilastik provides a stable result for all of the indicators tested, whether or not the signal is filtered. The comparison between Ilastik and standard image processing (filter + Otsu's method) very clearly shows the negative effects of the different algorithms on the edges and wedges when gray levels are similar, and the gray-level gradients are therefore very limited. The main consequence of this is that the sizes of both the large pores and the small pores are drastically reduced, and some pores are even eliminated, causing a constriction of the pores that can be seen in the coordination indicators and through the appearance of permeability anisotropy linked to filtering and slice-by-slice segmentation.

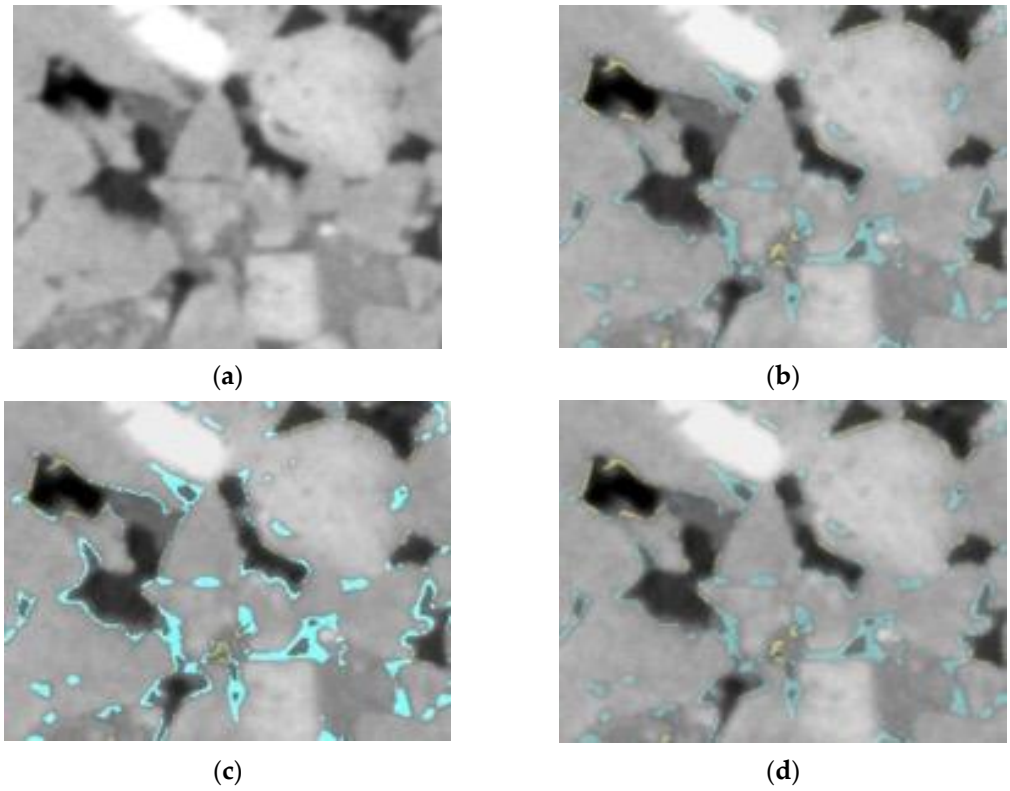

Figure 5. Impact and comparison at the local scale of the bilateral, Anisotropic Diffusion and Non-Local Means filters with Otsu's thresholding compared to Ilastik: (**a**) the raw reconstructed image with (**b**) the bilateral filter, (**c**) Anisotropic Diffusion, and (**d**) Non-Local Means. Local zooms with the voxels corresponding to voxels considered to represent porosity with Ilastik only (relative to the cited filter + Otsu's thresholding) in cyan; with the voxels corresponding to voxels considered to represent porosity with the cited filter + Otsu's thresholding only (relative to Ilastik) in yellow.

There were very marked differences between parameters such as specific surface, coordination number, and permeability, and this consequently had an effect on the conformance of the reconstructed pore space. This result is relatively intuitive for anyone interested in fluid flow in porous media. However, we demonstrated here that a difference of 3% in the porosity on the sample presented could generate differences of 10 to 15% in variables such as the coordination number and the specific surface area, and up to 30% in permeability.

Overall, applying filters when using Otsu's method reduced porosity by 3%. The edges and wedges, and therefore the totality of the interfaces and details, induced a displacement of the boundaries and the processing of details as noise.

Surprisingly, degradation of image quality when performing direct segmentation by multi-Otsu thresholding is no greater than when the signal is filtered using a high-quality light beam and 3D microscope. This observation is critical, because owing to the intrinsic quality of X-ray microscopes today (multi-axis stage, scintillators, optics, and detectors), images of excellent quality can be obtained. This result would have been different with older-generation tools, but it is clear that synchrotrons and laboratory X-ray microscopes now produce images that no longer require filtering, as long as the noise remains moderate and no reconstruction defects appear (ring artifact, beam hardening in white light). We also compared the results of segmentation performed by an experienced person and by a trainee, and found that the differences were even greater than those obtained when using the tools by themselves.

The 1% variations in porosity observed between the various standard filters had a strong impact on the physical characteristics of the porous medium and flow, since variations of 1% in porosity generate differences in specific surface area of 30 to 40% and variations in permeability of 8 to more than 30%.

Please note that Otsu segmentation of raw images gives rise to major unconformities despite a relatively close physical porosity, leading to some severe divergences. Porosity alone cannot reflect the accuracy of image processing, and we therefore conducted an extensive comparison of the local (image sampling) and global differences (indicators of morphology, topology and transport properties) observed for the main methods cited in the bibliography. For a 3% difference in porosity, the surface area and the coordination numbers were calculated to have an error range of about 10%, leading to a 30% difference in permeability. We also observed anisotropy when using the standard 2D filtering techniques, compared to the homogeneous permeabilities obtained when performing image processing using Ilastik.

4. Conclusions

With the advent of A.I. in image processing, phase classification has been significantly improved.

A filter can indeed reduce noise in an image by favoring the continuity of gray levels or gradients in the image, and where standard image processing uses one or two labels, A.I. techniques investigate multiple labels in order to propose optimized segmentations.

Benchmarked images clearly show that segmentation is improved, facilitated, faster (for the operator), and less affected by human inference in the search for the best compromise.

In the case of good- or excellent-quality images, the filtering step offers no advantages, and actually degrades the image quality by affecting the morphology of the pore space (shape), in particular the surface roughness and topology (connectedness), by eliminating the smallest pores. Based on these results, it appears that filtering must essentially be used to eliminate textured defects on images or certain specific defects causing a strong divergence of calculated or visualized results, such as very moderate ring artifacts, noisy images. As our experiment revealed, when using an efficient synchrotron-based 3D X-ray microscope, no preliminary filtering is required, as the segmentation step is performed by means of an efficient Artificial Intelligence algorithm such as Ilastik.

With multi-mineral rock types, the intermediate gradients strongly affect segmentation. The potassium iodide used as a contrast agent can be adjusted to optimize the contrast between minerals, and between water or oil for those interested in two-phase oil and gas systems.

However, in some complex cases, such as those described here, with multi-mineral rock types and two fluids in the pore space, properly identifying the phases is no mean feat. We clearly showed the impact of the segmentation method and the advantages of using Artificial Intelligence (A.I.) software integrating multiple classifiers. Of course, image processing is a decisive step, but all the other steps are equally important: experimental capability, reconstruction, and image processing. Several other techniques could be used to remove current limitations, and the solution undoubtedly resides in combining techniques, whether this involves enhancing phase identification or addressing the multiscale challenge.

We drew four main conclusions from this study:

- A synchrotron or even a 3D X-ray microscope produces high-clarity, contrasted raw tomographic images, in which noise is very much reduced compared to those obtained by conventional X-ray microtomography. The filtering step in this case is no longer required.
- The results obtained with Ilastik, as an A.I. multi-label segmentation software package, appear quite robust and relatively conform to those that an experienced scientist would obtain by performing a pixel-by-pixel classification.
- Some effective properties of the porous media are strongly affected by very small differences in porosity. We concluded that it was essential to define these properties for each image processing workflow in order to qualitatively and quantitatively determine error sensitivity in Digital Rock Physics. Given the results obtained, we can have every confidence in such a promising technique.

Unlike other methods, Ilastik offers a relatively robust image processing workflow and offers almost the same efficiency as an experienced scientist. The expertise and experience required for this method are less important than when using standard filters, where achieving the best compromise requires the adjustment of many parameters.

Future works will mainly focus on extending the methodology to a real 3D reconstruction rather than just 2D images (slice-by-slice) to exploit the continuity of the material along the z-axis and not just along x- and y-axes. We also plan to apply the method to other experimental set-ups comprising electron microscopes for example, and we intend to compare other image processing and A.I. algorithms.

Author Contributions: Conceptualization, R.G., M.V., G.D. and P.C.; methodology, M.N. and T.B.; Software, R.G. and G.D.; validation, M.N. and P.C.; formal analysis, M.N. and R.G.; investigation, R.G., M.N., M.V., T.B., G.D. and P.C.; writing—original draft preparation, R.G., M.V. and P.C.; writing—review and editing, R.G., M.V. and P.C.; supervision, P.C., R.G. and M.V.; project administration, P.C. All authors have read and agreed to the published version of the manuscript.

Funding: This research was initially supported as part of the Center for Nanoscale Control of Geologic CO2 (NCGC), an Energy Frontier Research Center funded by the U.S. 600 Department of Energy, Office of Science, Basic Energy Sciences under Award #DE-AC02-05CH11231. TOTALENERGIES is acknowledged for the funding and for scientific exchanges during the STEMS project.

Data Availability Statement: The data presented in this study are available on request from the corresponding author.

Acknowledgments: Alastair MacDowell and Dula Parkinson at the Advanced Light Source, Beamline 8.3.2, supported by the U.S. DOE Office of Science, Office of Basic Energy Sciences (DE-AC02-05CH11231) helped to operate the microXRT. The Advanced Light Source is supported by the Director, Office of Science, Office of Basic Energy Sciences, of the US Department of Energy (award No. DE-AC02-05CH11231). Jonathan Ajo-Franklin and Tae-Hyuk Kwon performed the original experiment. We especially acknowledge Alexandre Lapene and Eric Chaput for fructuous scientific exchanges. This work was granted access to the HPC resources of CALMIP supercomputing center under the allocation p21016.

Conflicts of Interest: The authors declare no conflict of interest. The funders had no role in the design of the study; in the collection, analyses, or interpretation of data; in the writing of the manuscript; or in the decision to publish the results.

References

1. Kumar, M.; Sok, R.; Knackstedt, M.A.; Latham, S.; Senden, T.J.; Sheppard, A.P.; Varslot, T.; Arns, C. Mapping Fluid Distributions in 3D at the Pore Scale: Quantifying the Influence of Wettability and Saturation History on Rock Resistivity. In Proceedings of the SPWLA 50th Annual Logging Symposium, The Woodlands, TX, USA, 21–24 June 2009.
2. Andrew, M.; Bijeljic, B.; Blunt, M.J. Pore-Scale Contact Angle Measurements at Reservoir Conditions Using X-ray Microtomography. *Adv. Water Resour.* **2014**, *68*, 24–31. [CrossRef]
3. Andrew, M.; Menke, H.; Blunt, M.J.; Bijeljic, B. The Imaging of Dynamic Multiphase Fluid Flow Using Synchrotron-Based X-ray Microtomography at Reservoir Conditions. *Transp. Porous Media* **2015**, *110*, 1–24. [CrossRef]
4. Voltolini, M.; Barnard, H.; Creux, P.; Ajo-Franklin, J. A New Mini-Triaxial Cell for Combined High-Pressure and High-Temperature *in Situ* Synchrotron X-ray Microtomography Experiments up to 400 °C and 24 MPa. *J. Synchrotron Radiat.* **2019**, *26*, 238–243. [CrossRef]
5. Voltolini, M.; Ajo-Franklin, J. The Effect of CO_2-Induced Dissolution on Flow Properties in Indiana Limestone: An in situ Synchrotron X-ray Micro-Tomography Study. *Int. J. Greenh. Gas Control* **2019**, *82*, 38–47. [CrossRef]
6. Guibert, R.; Nazarova, M.; Horgue, P.; Hamon, G.; Creux, P.; Debenest, G. Computational Permeability Determination from Pore-Scale Imaging: Sample Size, Mesh and Method Sensitivities. *Transp. Porous Media* **2015**, *107*, 641–656. [CrossRef]
7. Guan, K.M.; Nazarova, M.; Guo, B.; Tchelepi, H.; Kovscek, A.R.; Creux, P. Effects of Image Resolution on Sandstone Porosity and Permeability as Obtained from X-ray Microscopy. *Transp. Porous Media* **2019**, *127*, 233–245. [CrossRef]
8. Bear, J. *Dynamics of Fluids in Porous Media*; Elsevier: New York, NY, USA, 1972.
9. Kaestner, A.; Lehmann, E.; Stampanoni, M. Imaging and Image Processing in Porous Media Research. *Adv. Water Resour.* **2008**, *31*, 1174–1187. [CrossRef]
10. Schlüter, S.; Sheppard, A.; Brown, K.; Wildenschild, D. Image Processing of Multiphase Images Obtained via X-ray Microtomography: A Review. *Water Resour. Res.* **2014**, *50*, 3615–3639. [CrossRef]

11. Iassonov, P.; Gebrenegus, T.; Tuller, M. Segmentation of X-ray Computed Tomography Images of Porous Materials: A Crucial Step for Characterization and Quantitative Analysis of Pore Structures. *Water Resour. Res.* **2009**, *45*. [CrossRef]
12. Sheppard, A.P.; Sok, R.M.; Averdunk, H. Techniques for Image Enhancement and Segmentation of Tomographic Images of Porous Materials. *Phys. A Stat. Mech. Its Appl.* **2004**, *339*, 145–151. [CrossRef]
13. Gu, K.; Zhai, G.; Yang, X.; Zhang, W. Using Free Energy Principle for Blind Image Quality Assessment. *IEEE Trans. Multimed.* **2015**, *17*, 50–63. [CrossRef]
14. Gu, K.; Zhai, G.; Yang, X.; Zhang, W.; Chen, C.W. Automatic Contrast Enhancement Technology with Saliency Preservation. *IEEE Trans. Circuits Syst. Video Technol.* **2015**, *25*, 1480–1494. [CrossRef]
15. Anderson, T.I.; Vega, B.; Kovscek, A.R. Multimodal Imaging and Machine Learning to Enhance Microscope Images of Shale. *Comput. Geosci.* **2020**, *145*, 104593. [CrossRef]
16. Andrä, H.; Combaret, N.; Dvorkin, J.; Glatt, E.; Han, J.; Kabel, M.; Keehm, Y.; Krzikalla, F.; Lee, M.; Madonna, C.; et al. Digital Rock Physics Benchmarks—Part I: Imaging and Segmentation. *Comput. Geosci.* **2013**, *50*, 25–32. [CrossRef]
17. Andrä, H.; Combaret, N.; Dvorkin, J.; Glatt, E.; Han, J.; Kabel, M.; Keehm, Y.; Krzikalla, F.; Lee, M.; Madonna, C.; et al. Digital Rock Physics Benchmarks—Part II: Computing Effective Properties. *Comput. Geosci.* **2013**, *50*, 33–43. [CrossRef]
18. Saxena, N.; Hofmann, R.; Alpak, F.O.; Dietderich, J.; Hunter, S.; Day-Stirrat, R.J. Effect of Image Segmentation & Voxel Size on Micro-CT Computed Effective Transport & Elastic Properties. *Mar. Pet. Geol.* **2017**, *86*, 972–990. [CrossRef]
19. Voltolini, M.; Kwon, T.H.; Ajo-Franklin, J. Visualization and Prediction of Supercritical CO_2 Distribution in Sandstones during Drainage: An In Situ Synchrotron X-ray Micro-Computed Tomography Study. *Int. J. Greenh. Gas Control* **2017**, *66*, 230–245. [CrossRef]
20. Savage, N. Marriage of Mind and Machine. *Nature* **2019**, *571*, S15–S17. [CrossRef]
21. Tomasi, C.; Manduchi, R. Bilateral Filtering for Gray and Color Images. In Proceedings of the Sixth International Conference on Computer Vision (IEEE Cat. No.98CH36271), Washington, DC, USA, 4–7 January 1998. [CrossRef]
22. Perona, P.; Malik, J. Scale-Space and Edge Detection Using Anisotropic Diffusion. *IEEE Trans. Pattern Anal. Mach. Intell.* **1990**, *12*, 629–639. [CrossRef]
23. Dvorkin, J.; Derzhi, N.; Diaz, E.; Fang, Q. Relevance of Computational Rock Physics. *Geophysics* **2011**, *76*, E141–E153. [CrossRef]
24. Arganda-Carreras, I.; Kaynig, V.; Rueden, C.; Eliceiri, K.W.; Schindelin, J.; Cardona, A.; Seung, H.S. Trainable Weka Segmentation: A Machine Learning Tool for Microscopy Pixel Classification. *Bioinformatics* **2017**, *33*, 2424–2426. [CrossRef]
25. Berg, S.; Kutra, D.; Kroeger, T.; Straehle, C.N.; Kausler, B.X.; Haubold, C.; Schiegg, M.; Ales, J.; Beier, T.; Rudy, M.; et al. Ilastik: Interactive Machine Learning for (Bio)Image Analysis. *Nat. Methods* **2019**, *16*, 1226–1232. [CrossRef]
26. Sommer, C.; Straehle, C.; Köthe, U.; Hamprecht, F.A. Ilastik: Interactive Learning and Segmentation Toolkit. In Proceedings of the 8th IEEE International Symposium on Biomedical Imaging, Chicago, IL, USA, 30 March–2 April 2011.
27. Berg, S.; Saxena, N.; Shaik, M.; Pradhan, C. Generation of Ground Truth Images to Validate Micro-CT Image-Processing Pipelines. *Lead. Edge* **2018**, *37*, 412–420. [CrossRef]
28. Tschumperl, D. The Cimg Library. In Proceedings of the IPOL 2012 Meeting on Image Processing Libraries, ENS Cachan, France, 27 June 2012; p. 4. Available online: https://www.ipol.im/event/2012_imlib/ (accessed on 4 August 2022).
29. Franc, J.; Guibert, R.; Horgue, P.; Debenest, G.; Plouraboué, F. Image-Based Effective Medium Approximation for Fast Permeability Evaluation of Porous Media Core Samples. *Comput. Geosci.* **2021**, *25*, 105–117. [CrossRef]